RSC Advances

PAPER

View Article Online
View Journal | View Issue

Cite this: *RSC Adv.*, 2024, **14**, 32517

Dual nanofiber and graphene reinforcement of 3D printed biomimetic supports for bone tissue repair†

Elena Cojocaru,‡[a] Mădălina Oprea,‡[ab] George Mihail Vlăsceanu,[ab] Mădălina-Cristina Nicolae,[a] Roxana-Cristina Popescu,[bc] Paul-Emil Mereuţă,[d] Alin-Georgian Toader[ab] and Mariana Ioniţă*[abe]

Replicating the intricate architecture of the extracellular matrix (ECM) is an actual challenge in the field of bone tissue engineering. In the present research study, calcium alginate/cellulose nanofibrils-based 3D printed scaffolds, double-reinforced with chitosan/polyethylene oxide electrospun nanofibers (NFs) and graphene oxide (GO) were prepared using the 3D printing technique. The porous matrix was provided by the calcium alginate, while the anisotropy degree and mechanical properties were ensured by the addition of fillers with different sizes and shapes (CNFs, NFs, GO), similar to the components naturally found in bone ECM. Surface morphology and 3D internal microstructure were analyzed using scanning electron microscopy (SEM) and micro-computed tomography (μ-CT), which evidenced a synergistic effect of the reinforcing and functional fibers addition, as well as of the GO sheets that seem to govern materials structuration. Also, the nanoindentation measurements showed significant differences in the elasticity and viscosity modulus, depending on the measurement point, this supported the anisotropic character of the scaffolds. *In vitro* assays performed on MG-63 osteoblast cells confirmed the biocompatibility of the calcium alginate-based scaffolds and highlighted the osteostimulatory and mineralization enhancement effect of GO. In virtue of their biocompatibility, structural complexity similar with the one of native bone ECM, and biomimetic mechanical characteristics (*e.g.* high mechanical strength, durotaxis), these novel materials were considered appropriate for specific functional needs, like guided support for bone tissue formation.

Received 26th August 2024
Accepted 8th October 2024

DOI: 10.1039/d4ra06167e

rsc.li/rsc-advances

Introduction

It is estimated that, each year, more than 1.5 million people suffer a bone fracture or defect as a result of congenital anomalies, trauma, and diseases.[1] Despite the bone's intrinsic capacity for self-regeneration, large segmental defects (>2 cm, depending on the anatomical location) sometimes fail to heal and their treatment represents a significant clinical challenge.[2,3] The conventional approach for such large osseous defects is represented by allografts, xenografts or autografts. However, limited donor availability and high risk of infection led to the development of alternative methods, more specifically, biomaterial-based scaffolds for bone tissue engineering.[4] In order for a biomaterial to be considered appropriate for scaffold fabrication, it should possess some mandatory features such as biocompatibility, non-immunogenicity, non-toxicity, controlled porosity and good mechanical properties.[5] Moreover, to design an effective bone tissue engineering (BTE) scaffold, it is important to mimic the structure and composition of the native bone and the biophysical and biochemical cues specific to the bone ECM.[6]

Bone ECM is mainly produced by osteoblasts and it is a dynamic environment comprised of 40% organic (*e.g.* water, collagen, and non-collagenous proteins – γ-carboxyglutamate-containing proteins, proteoglycans, glycoproteins, small integrin-binding ligands N-linked glycoproteins), and 60% inorganic (*e.g.* trace elements, calcium-deficient apatite) components.[7] The inorganic part confers strength and stiffness, being responsible for the bone ability to withstand

---

[a] *Advanced Polymer Materials Group, National University of Science and Technology POLITEHNICA Bucharest, 1–7 Gh. Polizu Street, Bucharest 011061, Romania. E-mail: mariana.ionita@polimi.it*

[b] *Faculty of Medical Engineering, National University of Science and Technology POLITEHNICA Bucharest, 1–7 Gh. Polizu Street, Bucharest 011061, Romania*

[c] *National Institute for Research and Development in Physics and Nuclear Engineering "Horia Hulubei", Department of Life and Environmental Physics, 30 Reactor. Street, Magurele, Romania*

[d] *National Institute for Research and Development in Physics and Nuclear Engineering "Horia Hulubei", Department of Applied Nuclear Physics, 30 Reactor. Street, Magurele, Romania*

[e] *Center of Excellence in Bioengineering, National University of Science and Technology POLITEHNICA Bucharest, 6 Iuliu Maniu Boulevard, Campus Building, Bucharest 061344, Romania*

† Electronic supplementary information (ESI) available. See DOI: https://doi.org/10.1039/d4ra06167e

‡ E. Cojocaru and M. Oprea contributed equally to this work and share first authorship.

deformation, while the organic components provide toughness by allowing energy absorption.[8] Studies showed that bone ECM is similar to an anisotropic composite material where the crystallographic *c*-axis of the apatite crystals is aligned almost parallel to the collagen fibers as a result of epitaxial crystallization.[9] This preferential orientation of the apatite crystals, and the anisotropic organization of both collagen and apatite were recognized as important determinants of bone mechanical functions, such as stiffness and crack propagation behavior.[10] Moreover, the apatite crystals size, degree of crystallinity as well as the type and grade of collagen crosslinking were showed to influence cellular behavior in terms of migration, proliferation and differentiation.[8]

Further on, understanding the interactions between cells and ECM is essential for designing performant scaffolds for tissue regeneration. Several studies demonstrated that cells seeded in conventional polystyrene substrates do not manifest the same features and behavior as *in vivo* cells, mainly due to the differences between the biochemical and mechanical characteristics of culture plates and natural ECM.[11] Therefore, the development of biomimetic scaffolds is vital for the evolution of the BTE field. Nowadays, it is generally acknowledged that cells are influenced by various mechanical forces from their surrounding environment, such as the compression applied by adjacent cells or the stiffness of the ECM.[12] For example, durotaxis, or the directed migration and growth of cells based on the stiffness gradients of their ECM, is an important aspect that influences tissular development.[13] The cellular reaction mechanism is based on three processes – downstream mechanoresponses, mechano-transduction, and mechano-sensation. Briefly, when the cells are placed in a specific environment, big protein complexes bind the cytoskeleton to the substrate and the physical signals from the ECM are sensed and converted to biochemical cues that induce changes in shape, growth, differentiation, migration and apoptosis. Also, it was observed that stem cells seeded in scaffolds with Young's modulus matching that of native ECM of brain (1–3 kPa) or bone (15–40 GPa), expressed the precursor genes of the cell lineage specific to those tissue types.[14,15]

Over the last twenty years, anisotropic porous scaffolds proved their efficiency in BTE, the currently used bone substitute being polymer/ceramic composites with biomimicking properties.[16,17] Naturally-derived polysaccharides (*e.g.* chitosan, hyaluronic acid, alginate) particularly, attracted a lot of research interest due to their native biocompatibility, biodegradability, structural similarity with the bone ECM and biochemical affinity towards ECM macromolecular components.[18] Amongst them, sodium alginate (SA), an anionic polysaccharide extracted from brown seaweed (*e.g. Laminaria hyperborea*, *Laminaria digitata*, *Macrocystis pyrifera*), was certified by the Food and Drug Administration (FDA) owing to its chemical similarity to ECM components, this ensuring promising results in the tissue engineering area.[14] Still, its major disadvantages are related to inferior mechanical strength in comparison with bone ECM, low stability in physiological conditions and potential functionality loss during manufacturing and storage.[19] Thus, by combining SA with inorganic components (*e.g.* metallic nanoparticles), natural or synthetic polymers, or functional fillers (*e.g.* cellulose nanofibrils, carbon nanotubes, graphene oxide), its mechanical characteristics and physicochemical stability are brought closer to the ones of bone tissue.[20] Cellulose nanofibrils (CNFs) are considered some of the most promising functional fillers for the reinforcement of alginate hydrogels owing to their sustainability, biocompatibility, good mechanical properties and abundance of surface hydroxyl groups that ensure effective interactions with polymeric matrices.[21] Several studies investigated the potential of SA/CNFs composites as scaffolds for BTE, in all cases an improvement in the rheological properties and mechanical strength of the hydrogels being observed, as well as favorable biomineralization capacity, osteogenic activity and good cytocompatibility.[22–24] Due to its physical, chemical and mechanical properties, graphene oxide (GO) is also viewed as an ideal filler for alginate-based BTE scaffolds.[25–27] Also, the abundant surface functional groups (*e.g.* –OH, –COOH) facilitate the chemical modification of GO to promote cellular adhesion, proliferation and differentiation into osteogenic lineages.[28] Moreover, it was showed that GO and nanostructured cellulose-based materials, such as CNFs, synergistically interact when they are used together for the synthesis of composite polymer scaffolds, their combined benefits outperforming those of each individual component.[3]

The purpose of this study was to synthesize calcium alginate-based BTE scaffolds, with anisotropic structure replicating the one of native bone ECM, for enhanced mineralization and cellular proliferation. The scaffolds were produced *via* 3D printing, a revolutionary technique that allows the fabrication of highly customizable 3D artificial constructs with finely controlled biomimetic geometries, specific to the targeted application.[29] The porous architecture was ensured by the calcium alginate component, while the mechanical properties and chemical stability were enhanced by reinforcing the polymer with CNFs and GO. For further improvement of the mechanical features and to replicate the anisotropic architecture of native bone ECM, chitosan/polyethylene oxide electrospun nanofibers (CS/PEO NFs) were added within the scaffolds' composition. To the best of our knowledge, there are no previous studies concerning this type of ECM-mimicking 3D printed anisotropic scaffolds, based on calcium alginate/CNFs double reinforced with NFs and GO, for bone tissue engineering applications. Previous research showed that CS/PEO NFs possess osteoconduction and osseointegration potential and excellent affinity for osteoblasts, that translates into improved cellular proliferation and growth, as well as in the upregulation of osteogenic genes expression.[30,31] PEO serves primarily to enhance the electrospinning process and improve the mechanical properties of the nanofibers. It aids in creating nanofibers that are thin yet strong, providing a fibrous texture similar to collagen fibrils in the bone ECM. The electrospun nanofibers offer a high surface-area-to-volume ratio, which is beneficial for cellular attachment and proliferation, like the fine fibrous network in the natural bone ECM. These fibers can also provide mechanical reinforcement to the overall scaffold, improving its ability to mimic the load bearing function of bone. In addition, the presence of these electrospun nanofibers enhances the scaffold's hierarchical architecture, similar to the features of natural ECM, which has multiple layers and fibers arranged in a highly organized manner. This multi-scale architecture promotes better cell adhesion, migration, and differentiation, which are key processes in bone tissue regeneration. Moreover, CS/PEO NFs were found to be an appropriate template for deposition of calcium phosphate crystals, the results being comparable to the ones of natural biomineralization.[32] In this regard, it was postulated that the nanometric size and geometry of NFs could replicate the naturally occurring collagen fibers from bone ECM, thus providing a biomineralization and cellular attachment template. Also, the durotaxis characteristic to native bone ECM is provided by both CNFs and GO components, which create areas with high mechanical strength necessary for cellular migration and differentiation towards the osteoblast lineage. In this study, we present a novel concept of composite scaffolds with good biocompatibility and harmonious distribution of stresses and strains across their structure, as a result of their physicochemical properties and geometrical configuration of the fillers, for specific functional applications such as guided support for bone tissue formation and regeneration.

Experimental procedure

Materials

Sodium alginate (SA), calcium chloride ($CaCl_2$, anhydrous, granular ≤ 7 mm, ≥93% purity), graphene oxide (GO, powder, 15–20 sheets, 4–10% edge-oxidized), chitosan (CS, medium M_w and deacetylation degree of 75–85%), polyethylene oxide (PEO, M_w of 900 kDa), and glutaraldehyde (GA, grade I, 50% aqueous solution) were acquired from Sigma-Aldrich. Cellulose nanofibrils (CNFs) were produced by treating never-dried bleached kraft pulp from softwood (generously provided by StoraEnso™) using a 2,2,6,6-tetramethyl-1-piperidinyloxy (TEMPO)-mediated oxidation process.[33] This resulted in gel-like CNF suspensions with a solid content of 1.2% (w/v). In all experiments, only ultrapure water obtained from Milli-Q Plus system was used.

Formulation of polymeric precursor inks in order to print the NFs and GO-co-loaded calcium alginate/CNF composites

The printable precursor inks were prepared by blending calcium alginate (A) solution and CNF gel (AC) in a 3/1 (v/v) ratio, with the remark that A solution was obtained by dissolving 5% (w/v) sodium alginate in a 0.3% (w/v) $CaCl_2$ aqueous solution, with magnetic stirring at 60 °C. This ink was used as control.

Next, the nanofibrous component (NFs) was added to the previously prepared ink formulation (ACN) in a percentage of 2% (w/w) of the total polymer mass, with prior manual crushing and ultrasonication (ultrasonic processor UP100H, 80% amplitude), in an ice bath for 1 hour, to ensure a good dispersion of NFs within the polymer matrix. Briefly, NFs were synthesized through the electrospinning process starting from a precursor solution containing both natural polymer (CS) and synthetic polymer (PEO) in a CS/PEO (w/w) ratio of 3/7; due to the polycationic character of CS, it is quite difficult to electrospun alone. Then, the nanofibrous meshes were chemically crosslinked in glutaraldehyde vapors and vigorously washed with ultrapure water, as described in our previous paper.[30]

Subsequently, in order to achieve the composite ink formulations, the graphene component (GO) was also incorporated within the NFs-containing ink (ACNG), in various concentrations with respect to final volume of the polymer solution (w/v), followed by ultrasonication treatment in an ice bath for 2 hours. The multicomponent inks thus prepared were coded and depicted in Table 1.

3D printing parameter optimization and fabrication of 3D NFs/GO-co-loaded calcium alginate/CNF composites

Before printing, all formulated inks were subjected to ultrasonication treatment using an ultrasonic processor (30 minutes, 80% amplitude), to assure their homogeneity. Then, they were charged into 3 mL cartridges equipped at the bottom with a 22 G metal needle (inner diameter of 0.41 mm and length of 6.35 mm), and at the top with a tube that provides the necessary pressure for the precursor extrusion through the needle. The cartridge was fitted to the direct dispensing-based printhead (*XYZ* moving arm) of the BIO X6 3D bioprinter (Cellink, Gothenburg, Sweden), and the printing process took place at room temperature (25 ± 3 °C) by depositing the formulated ink on a Petri dish. The 3D materials were printed in a controlled layer-by-layer manner, using the optimized printing parameters for each ink formulation (Table 1), such as pneumatic pressure and printing speed, by means of DNA Studio V4 1.3 specific software of the 3D bioprinter. The 3D cube models with the (length × width × height) of 10 × 10 × 1 mm,

Table 1 Multicomponent precursor ink formulation and printing parameter optimization

Ink code	A (% w/v)	CNF (% w/v)	NFs (% w/w)	GO[a] (% w/v)	Pneumatic pressure (kPa)	Printing speed (mm s^{-1})
A	5	—	—	—	100–120	6–7
AC	5	1.2	—	—	100–110	7–9
ACN	5	1.2	2	—	70–100	7–9
ACNG-0.1	5	1.2	2	0.1	130	8–9
ACNG-0.2	5	1.2	2	0.2	110–120	8
ACNG-0.5	5	1.2	2	0.5	110–120	8

[a] With respect to final volume of the polymer solution (w/v).

$10 \times 10 \times 3$ mm, $10 \times 10 \times 5$ mm, infill pattern of grids and infill density of 32%, were imported into the software, in the form of STL files. All the 3D printed scaffolds were subsequently immersed in a 2% (w/v) $CaCl_2$ aqueous solution and kept for 10 minutes for ionic gelation, followed by vigorous washing with ultrapure water to remove unreacted Ca^{2+} ions. For further investigations, the materials thus prepared were frozen at −20 °C overnight and freeze-dried at a −90 °C temperature and 0.05 mbar pressure for 24 hours.

Rheological characterization

Rheological data were obtained using a Kinexus Pro rheometer (Malvern Panalytical Ltd., UK), which was equipped with a Peltier element for temperature control and a parallel plate geometry with a diameter of 20 mm. Viscosity as a function of shear rate was investigated by measurements at constant shear stress in the shear rate interval 0.01 and 1000 s^{-1}. Dynamic oscillatory measurements were made in amplitude sweep and frequency sweep. In the amplitude sweep, the frequency was set constant at 1 Hz. With oscillatory tests, the storage (G') and loss (G'') moduli were determined in the linear viscoelastic region (LVR) with frequency sweeps varying from 0 to 10 Hz. The formulated inks were positioned on the base plate, and the top plate was lowered to establish a fixed gap of 0.5 mm. All types of measurements were done in triplicate at room temperature (25 °C), and a water-lock system was employed to prevent the samples' dehydration.

Printability evaluation

The optimal printing parameters must be chosen to assess the formulated inks' printability and produce high-quality scaffolds with fine shape fidelity. The 3D scaffolds with dimensions of $10 \times 10 \times 3$ mm were printed using a 22 G metallic needle (0.41 mm inner diameter), at different extrusion pressure (depending on ink composition-see Table 1) with a printing speed of around 8 mm s^{-1}. The following factors were used to evaluate the inks' printability: printability index,[34] expansion ratio[35] and uniformity factor.[36]

The printability index (P_r) of each formulated ink was assessed to determine the shape fidelity of the printed scaffolds, by means of the eqn (1):

$$P_r = \frac{p^2}{16 \times A} \tag{1}$$

where A is the pore area and P is the pore perimeter. The optical micrographs of every printed support were randomly selected for this investigation. ImageJ software (version 1.54 d) was used to determine the P_r of the randomly taken optical images by calculating the pore area and perimeter of each pore ($n = 5$). The consistency of the printed features was evaluated by analyzing the dimensions of the strands in the optical images through image analysis.[37]

The average extrusion of the ink upon exit the needle tip owing to fluid shear stress, is what determines the expansion ratio (α). During the extrusion process, the filament diameter exceeds that of the needle. The ink composition, needle diameter (D), filament diameter (d), and flow rate have a significant impact on the expansion degree. The eqn (2) may be used to calculate the expansion ratio:

$$\alpha = \frac{d}{D} \tag{2}$$

The printed structure's uniformity with the conceptual layout was assessed using the uniformity factor (U), which was calculated as the ratio between length of the printed strand (L_p) and length of the theoretical design (L_t), using the eqn (3):

$$U = \frac{L_p}{L_t} \tag{3}$$

Morphological investigations

Internal microstructure of 3D printed scaffolds was visualized through micro-computed tomography (μ-CT) using a SkyScan 1272 high resolution equipment. Each dataset was obtained by scanning the freeze-dried prints, after they was affixed to a holder using modelling paste, in front of the source of 50 kV voltage and 200 μA current, during a 180° rotation with a rotation step of 0.2°. 3D representations were recorded with an image pixel size (scanning resolution) of 1.5 μm. Afterward, the data were processed using the CT NRecon software (Bruker) and reconstructed into micrographs of 3D objects using CT-Vox.

The morphological characteristics of the samples were investigated using a Hitachi TM4000plus II Scanning Electron Microscope (SEM) (Hitachi, Tokyo, Japan) and the TM4000 software (version 1.5). The surface morphology was investigated by detecting the backscattered electrons (BSE) signals in conductor operation mode (3–5 Pa), using 15 kV as the accelerating voltage. Prior to the SEM analysis, the freeze-dried scaffolds were fixed on a metallic stage with carbon tape and coated with a conductive thin gold layer (6 nm thickness) using the SEM coater equipment LUXOR Au/Pt (IB-FT GmbH, Berlin, Germany).

Structural analysis

Fourier Transform Infrared (FTIR) spectra of all analyzed samples were recorded using a Bruker Vertex 70 FTIR spectrometer (Bruker, Billerica, MA, USA), featuring an attenuated total reflectance (ATR) accessory. The spectra covered the wavenumber range of 4000 to 600 cm^{-1}, with a resolution of 4 cm^{-1}, and 32 scans were conducted for each sample. FTIR spectra were processed using Omnic 9 software.

Nanomechanical properties evaluation

The scaffolds nanomechanical characteristics were investigated using the nanoindentation technique by means of a Nano Indenter G200 equipment (Keysight Technologies, USA), configured with a DCM head and a continuous stiffness measurement (CSM) option. The "G-Series DCM CSM Flat Punch Complex Modulus, Gel" method from NanoSuite software (version 6.52.0) was employed to carry out the measurements of storage (G') and loss (G'') moduli. A DCM II diamond flat-punch indenter tip with radius of 97.7 μm was used. The parameters, such as testing frequency, pre-compression test, and Poisson ratio were set to 110 Hz, 5 μm and 0.5, respectively. Ten different indentations separated by at least 500 μm were performed on each sample.

Thermal behavior

Differential scanning calorimetry (DSC) was employed to analyze the thermal behavior of the alginate-based materials using a NETZSCH 204 equipment. 20 mg of each sample were placed into aluminum pans, and the analysis was performed under nitrogen atmosphere (99.99% purity) with a 5°C min^{-1} heating rate.

In vitro swelling studies

In vitro swelling experiments were carried out in water with pH 7.4 at 37 °C (under physiological conditions), in order to assess the rehydration capacities of the 3D printed scaffolds. Each sample was lyophilized before being weighted (w_0) and placed into 10 mL of PBS. At specified intervals, the scaffolds were removed from the medium, carefully wiped using absorbent paper to remove any remaining liquid, and then weighed in the swelling state (w_s). When the masses of the samples remained unchanged after two consecutive weightings, the maximum swelling degree (MSD) was taken into account. Each sample's swelling degree (SD) was calculated using eqn (4):

$$\text{SD }(\%) = \frac{w_s - w_0}{w_0} \times 100 \tag{4}$$

In vitro degradation studies

In vitro degradation behavior of the composite scaffolds was examined using the following procedure. The tests were achieved in water with pH 7.4, at 37 °C, mimicking the physiological conditions. The lyophilized samples were weighed before being introduced into the medium (w_0), then after every 24 hours, the scaffolds were taken out from medium, dried by lyophilization, and weighed again (w_d). The degradation degree (DD) was calculated using eqn (5):

$$\text{DD }(\%) = \frac{w_0 - w_d}{w_0} \times 100 \tag{5}$$

In vitro evaluation of cellular response

The MG-63 osteoblast cells (CLS, Heidelberg, Germany) were used for *in vitro* investigation considering the materials are foreseen for bone tissue regeneration. MG-63 osteoblast cells were cultured in Dulbecco's Modified Eagle Medium (DMEM), supplemented with 10% bovine fetal serum and 1% penicillin–streptomycin, under standard temperature and humidity conditions (37 °C, 5% CO_2, 90% humidity). The cells were seeded at a concentration of 100 000 cells per 500 μL per well, in a 24 wells plate, and incubated under standard temperature and humidity conditions, for 24 hours, to allow cellular adhesion. The calcium alginate-based scaffolds were sterilized under UV exposure, for 1 hour on each side. After sterilization, the samples were placed in direct contact with the MG-63 cells and incubated for another 4, 7 and 14 days, respectively. The culture medium was filled with an additional 2 mL, so that the samples were completely immersed. The cells were incubated under standard temperature and humidity conditions and, afterwards, investigations regarding cellular viability and differentiation were performed.

After the initial incubation period, 50 μL of supernatant from each well was collected and added to a new 96 well plate, to measure the amount of LDH released by the cells upon interaction with the biomaterial samples. LDH is a cytosolic enzyme, which acts as a catalyst in the lactate metabolization reaction to pyruvate. LDH is released into the extracellular environment only as a result of cell membrane ruptures, therefore extracellular LDH is a measure of cell death by necrosis. To measure LDH released by the cells because of exposure to the scaffolds, the CyQUANT LDH Cytotoxicity Assay (Invitrogen, Thermo Fisher Scientific, Waltham, Massachusetts, USA) was used. The samples were prepared according to the manufacturer's specifications (by incubation with a series of reagents), and the absorbance was measured at 490 nm wavelength. The amount of LDH released was calculated by reference to the negative control (cells that were not exposed to the samples).

Cellular viability investigations were performed using the (3-(4,5-dimethylthiazol-2-yl)-2,5-diphenyltetrazolium bromide) or MTT assay. The MG-63 cells were incubated with an MTT solution, prepared by dissolving 10% MTT (5 mg mL^{-1} in PBS) in complete DMEM culture medium, for 2 hours, under standard conditions. This assay investigates the cellular metabolic activity as an indicator of cellular viability and it is based on the reduction of yellow tetrazolium salts to purple formazan crystals by metabolically active cells.[38] After the incubation time, the MTT culture medium was removed, and the formazan crystals were solubilized with DMSO. The amount of formazan was determined by spectrophotometric measurements of the absorbance at 570 nm wavelength. Cellular viability was calculated by reporting the data obtained for each sample to the negative control (which was assigned a value of 100%).

Cellular differentiation was highlighted by measuring the mineralization degree of the cell cultures following exposure to the analyzed samples *via* Alizarin Red staining of Ca deposits. After the incubation period, the samples were removed and the cells were washed with PBS and fixed with 3.7% paraformaldehyde in PBS, overnight, at 4 °C. Next, the cells were washed with PBS, stained with a 40 mM Alizarin Red solution, and, after 45 min, they were washed thoroughly with deionized water to remove any traces of unreacted dye. Further on, the cells were incubated with a 10% acetic acid solution to dissolve the dye that reacted with the Ca deposits, for 1 h, by horizontal shaking. The supernatant from each sample was collected in an Eppendorf tube, sealed with mineral oil and incubated for 10 minutes at 85 °C, to facilitate the dissolution process. The resulting solution was collected in new tubes and the acetic acid was neutralized with a 10% ammonia solution. The absorbance of the resulting solution was measured at 405 nm wavelength and the results were obtained by referring the absorbance of each individual sample to the absorbance of the negative control. The negative control (NC) was represented by cells incubated only with complete culture medium and the positive control (PC) was represented by 1% Triton-X in complete culture medium.

For cell adhesion investigations using scanning electron microscopy, 100 000 cells per 500 μL were seeded directly onto each scaffold and incubated during 30 minutes in standard conditions of temperature and humidity. Afterwards, up to 2 mL of cell culture media were added onto each corresponding well. The samples were incubated for additional 4 days in standard conditions. Following the incubation time, the samples were washed with PBS, fixed with 2.5% glutaraldehyde in PBS for 1 h, washed with PBS and dehydrated by immersion in ethanol and ethanol/hexamethyldisilazane of increasing concentrations. The imaging was done using a Zeiss EVO MA15 SEM (4 nm resolution at 30 kV acceleration voltage).

Statistical analysis

All results represent the average values of three measurements, along with their standard deviation (mean ± S.D.). Statistical analyses were accomplished using the one-way or two-way ANOVA test from GraphPad Prism 8.0.1 software (GraphPad Inc., USA). Differences were considered significant when $p < 0.05$.

Results and discussion

Rheological evaluation

Pseudo-plasticity, also known as shear-thinning behavior, refers to a decrease in viscosity with an increase in shear rate and represents the fundamental property of a material to be used in extrusion-based 3D printing. This behavior is a consequence of the ability of some colloids to orient in the flow direction when a shear rate is applied. Fig. 1A shows the relationship between shear stress and shear rate, and it can be observed that the shear stress increases with the shear rate. The appearance of a curvature in the case of A ink is due to the weak ionic gelation of sodium alginate with $CaCl_2$ solution before printing, which disrupts the structure with increasing shear rate. The flow curves of the inks are shown in Fig. 1B as a plot of viscosity *versus* shear rate. All precursor compositions exhibit a shear thinning behavior, a property that governs the inks' printability in extrusion-based printing. It may also be observed that the viscosity and shear thinning behavior of the formulated inks are influenced by their composition.

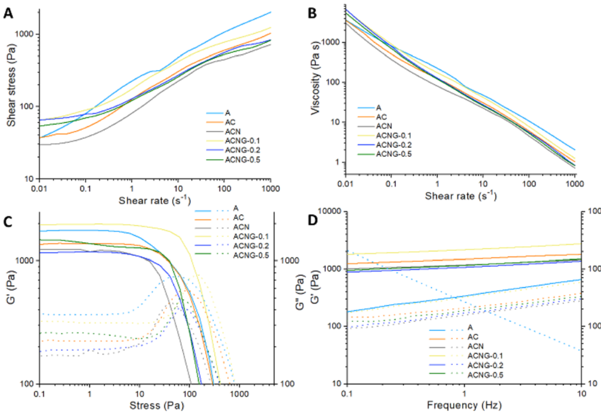

Fig. 1 Rheological results: (A) shear stress and (B) viscosity as a log–log function of shear rates for the formulated inks; elastic and viscous moduli (G' and G'') *versus* (C) stress and (D) frequency for precursor composite inks.

The A ink presented the least shear thinning behavior, while the ink with 0.1% GO (ACNG-0.1) exhibited the highest value of viscosity in the interval 0.01–0.1 s^{-1}; this increased viscosity is related to the rise of solid components within the ink structure, which leads to the appearance of non-covalent interactions with the formation of hydrogen bonds between polymer chains and GO. During the entire investigated interval, the ACN ink presented the smallest value of viscosity, which may suggest that the addition of NFs diminishes the interaction between calcium alginate and CNFs.

Viscosity experimental data were also used to obtain quantitative information on the investigated inks. The Herschel–Bulkley model (eqn (6)) was selected for fitting the flow curves, which describe non-Newtonian fluids:

$$\tau = \tau_0 + Kx^n \tag{6}$$

where τ is the shear stress (Pa), τ_0 is the yield stress (Pa), K is the consistency index (Pa s^n), x is the shear rate (s^{-1}) and n is the flow behavior index.

The values of the model parameters obtained by the interpolations in the domain 0.1–100 s^{-1} for the studied materials are reported in Table 2. The correlation coefficient values (R^2) are bigger than 0.994 for the Herschel–Bulkley model, showing a good fit of the data. The flow behavior index (n) measures the pseudoplastic or dilatant behavior of a fluid, where values of $n < 1$ are associated with shear-thinning behavior; the lower value of n, the more pronounced the shear-thinning behavior. A decrease in n value can be observed with the components' addition within the ink, which could be explained by a shear rate-induced rupture within the polymer networks and the alignment of materials because of the surface interactions between CNFs, NFs, and GO in the flow direction. Nonetheless, instead of further decreasing the flow behavior index, raising the GO concentration to 0.5% indicates that the surface interaction between components tends to diminish due to the GO agglomeration. The yield stress (τ_0), a requirement for extrusion control, represents the required force with which the material

Table 2 Rheological parameters of studied inks from Herschel–Bulkley model and values of loss tangent at 0.25 Hz

Ink code	τ_0 (Pa)	K (Pa s^n)	n	R^2	Tan(δ)
A	64.86	146.35	0.42	0.994	—
AC	24.37	106.44	0.38	0.995	0.159
ACN	0	100.27	0.34	0.994	0.154
ACNG-0.1	0	213.06	0.28	0.994	0.174
ACNG-0.2	0	189.70	0.19	0.993	0.123
ACNG-0.5	0	166.73	0.22	0.995	0.127

will flow like a liquid. It was observed that with the addition of NFs, τ_0 became 0, which determines a not very well controlled extrusion process. The consistency index (K) is a parameter related to interactions and structural stability; lower values determine the loss of shape fidelity with the addition of layers. The K values are highly influenced by the inks' composition; the highest value is reached by the ACNG-0.1 ink, which could be explained by the existence of stronger interactions between components, indicating the use of an optimal GO concentration.

The amplitude sweeps were investigated to determine the linear-viscoelastic region (LVR) of the inks (Fig. 1C) and the viscoelastic behavior. It is known that values of storage modulus (G') higher than those of loss modulus (G'') indicate a solid-like behavior, while G' lower than G'' is related to liquid-like behavior. To be printed, the ink must have a solid-like behavior to support its weight with an increase in layers' number. The investigated inks exhibit a gel-like behavior with G' greater than G'' in the LVR; the ACNG-0.1 ink showed the largest LVR interval, whereas for the A ink, the LVR was smaller. At high shear stress, G' and G'' intersect and represent the point at which the interactions between components are broken, and the ink has a liquid-like behavior.

Frequency sweeps were made to obtain values for loss tangent ($\tan(\delta)$) and to investigate the inks' behavior. As can be seen in Fig. 1D, all compositions, apart from the A ink, presented a small dependence of modulus with frequency, which indicates that the compositions behave as solid-like gels, with the G' bigger than the G'', which will ensure the shape fidelity.[39] At low frequency (less than 1 Hz), the A ink presented a liquid-like behavior with G'' higher than G', which will make this composition to be difficult to print. It can be considered that the addition of CNFs is responsible for the solid-like gel behavior, which is in good agreement with frequency sweeps data. The data also showed that G' increased about 100 times compared to the G' of A ink, with the CNFs addition. After the NFs incorporation, the G' slightly decreased, which may be attributed to the fact that its use did not lead to the formation of electrostatic interactions between the formulations' components. The highest value of G' was reached by ACNG-0.1 ink, which may be attributed to the formation of many electrostatic interactions and hydrogen bonds between the functionalities of calcium alginate, CNFs, NFs, and GO. Conversely, the G' decreases with the rise of GO concentration, which can be attributed to a rearrangement of the polymeric chain entanglements. Considering the large LVR interval and high G' obtained in the case of ACNG-0.1 ink, it can be concluded that the optimal concentration of GO is 0.1%.

The values of $\tan(\delta)$ at 0.25 Hz frequency are presented in Table 2, except for A ink, which is considered to be non-printable. Values of $\tan(\delta)$ have been reported to directly influence the scaffold shape retention; it is considered that a value of approximately 0.2 is critical to ensure ink printability.[40]

Based on this regard, the best printability is exhibited by the ACNG-0.1 ink, having a δ value of 0.174, and followed by AC > ACN > ACNG-0.5 > ACNG-0.2. Numerous studies have shown that when GO sheets are used in polymer matrices, they can be uniformly distributed or agglomerated depending on the concentration used.[41–43] When the GO sheets are uniformly distributed, the mechanical properties are improved. In this case, using a concentration of 0.1% leads to a uniform and random distribution with the formation of strong hydrogen bonding between GO and biopolymeric matrix, while using more than 0.2% results in the formation of some aggregates of GO sheets, which acts as material defects, thus reducing the mechanical properties which was also observed by Li J. *et al.*[44] Similarly, the occurrence of GO sheets agglomeration may lead to the nozzle clogging during printing process which may lead to the ink instability.[45]

Ink printability assessment

Using an extrusion-based 3D printer, several ink formulations were printed onto 10 × 10 × 3 mm 3D constructs with a grid structure. Fig. 2A shows the optical images of the 3D scaffolds before gelation, along with the insets on the right side that represent the filament drop test for each ink, immediately after the actual printing. Fig. 2B illustrates the optical images of ionically gelated 3D scaffolds.

The filament drop test was used to investigate the structure, stability and geometry of the filaments. The results showed that the AC ink presented the best printing properties according to the P_r index value of 1.03 ± 0.04 (Fig. 2C), owing to the presence of CNF within the precursor composition, which presents shear thinning properties and gel-like networks that stop the printed layers from collapsing or deforming and help to keep the shape fidelity during the printing process.[46] The AC precursor formed a uniform and continuous filament, which maintained its geometry during the extrusion, compared to the A ink, which formed a slightly uneven filament along its entire length, and the ACN ink, which presented a textured and non-uniform filament, probably due to the presence of CS electrospun

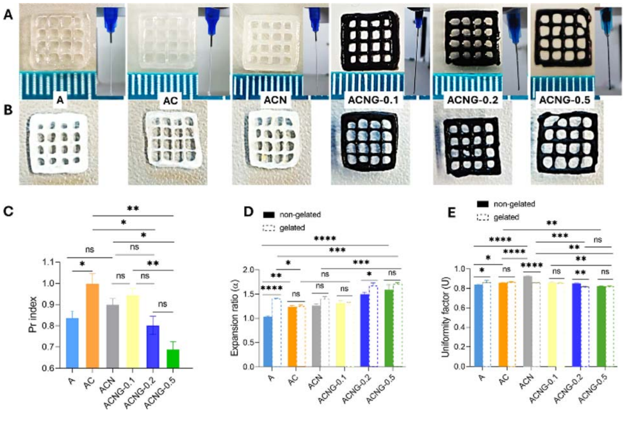

Fig. 2 Printability evaluation of the formulated inks. Optical images of the printed grid structures (inset is represented the filament drop test for each ink) (A) before and (B) after ionic gelation; (C) printability index of the inks (ns $p > 0.5$, *$p < 0.05$, **$p > 0.001$); (D) expansion ratio of filament diameter with and without gelation conditions (ns $p > 0.5$, *$p < 0.05$, **$p > 0.001$, ***$p < 0.005$, ****$p < 0.0001$); (E) uniformity factor of the inks with and without gelation conditions (ns $p > 0.5$, *$p < 0.05$, **$p < 0.005$, ***$p < 0.0005$, ****$p < 0.0001$).

nanofibers. Regarding the P_r index, there are insignificant differences between the A (0.85 ± 0.03) and ACN (0.92 ± 0.03) inks.

From the printability point of view, the AC precursor was followed by ACNG-0.1 (P_r index of 0.96 ± 0.03), which exhibited a continuous, uniform, and stable filament, despite the addition of 0.1 wt% GO. Later, increasing the GO content within the ACNG-0.2 and ACNG-0.5 inks, they formed irregular, discontinuous, and unstable filaments, with a tendency to aggregate at the bottom during extrusion; these results are consistent with the P_r index of the two precursors (0.83 ± 0.04 for ACNG-0.2 and 0.71 ± 0.03 for ACNG-0.5), which suggest poor printing capabilities; therefore, the P_r index decreases with increasing GO concentration within the materials composition. Moreover, the printability results were slightly different from tan(δ) values obtained from rheological data, which predicted that the best printability will be in the case of ACNG-0.1 ink, followed by AC ink. This difference could be attributed to the exceptional mechanical properties of GO, which will lead to an increase in G', without having any significant impact on the improvement of the extrusion process. However, in the case of GO-containing inks, the rheological data predicted the optimal GO concentration for printing, which correlates with the printability tests.

The printability evaluation of precursor inks was further conducted using the following factors: printability index (P_r), expansion ratio (α) (Fig. 2D), and uniformity factor (U) (Fig. 2E). Subsequently, the effect of ionic gelation on the expansion ratio and uniformity factor of the 3D printed materials was investigated. Fig. 2D exhibits the α for non-gelated and gelated materials; the filament expansion degree both before and after gelation is indicated by the α value. The findings showed that the α values differed between both non-gelated and gelated structures. For non-gelated samples, the α value gradually increased with the rising GO concentration. A similar trend was also observed in the gelated ones, suggesting a stronger interaction between the formulation components, which promotes the creation of a viscous ink. For each of the various inks, U was calculated for a single layer of the whole construction. The results are expressed in Fig. 2E, showing that the gelation step had minimal effect on the strands' length. Instead, it was observed that the U of GO-containing samples (especially ACNG-0.2 and ACNG-0.5) significantly decreased compared to the ACN ink, both in the case of non-gelated and gelated samples. This was likely due to the uneven dispersion and agglomeration of GO sheets, which also made the printing process more difficult, as shown in the optical images presented in Fig. 2A and B.

Morphological investigations by SEM analysis

Surface morphology and porosity are important features of tissue engineering scaffolds. Studies showed that scaffolds with pore size of 200–500 μm have the best performances in hard tissue regeneration, and, in order to facilitate nutrients' transfer and osteoconduction, the minimum pore size should be at least 100–150 μm.[47] The top view, surface and cross-section SEM micrographs of the calcium alginate-based scaffolds are presented in Fig. 3. The top-view images (Fig. 3A) revealed that the geometrical features fixed in the design stage were accurately reproduced in the final products and the initial shape was well maintained after the freeze-drying process. Regarding scaffolds morphology, the materials showed a rough, irregular surface that mimics the aspect of natural bone ECM. The neat sample (A) showed an inhomogeneous surface aspect, characterized by a porous architecture with large and interconnected pores. After the addition of CNFs (AC) and NFs (ACN), the surface roughness was significantly increased, and the materials showed a folded-sheet-like morphology (Fig. 3B). A similar phenomenon was observed by Nakayama *et al.* in the case of composite calcium alginate/CNFs membranes, which was attributed to the formation of hydrogen bonds between the polymer matrix and organic filler, and also to the increase in the degree of crystallinity.[48] Furthermore, the morphological changes could also be related to the electrostatic interactions between the –NH_3^+ groups from chitosan structure and the –COO^- ones from calcium alginate.[49] Considering the rheology and FTIR results (Fig. 5), the occurrence of electrostatic interactions and hydrogen bonds between the formulation components was most likely the reason for the morphological changes noticed in the SEM micrographs of the composites. This surface

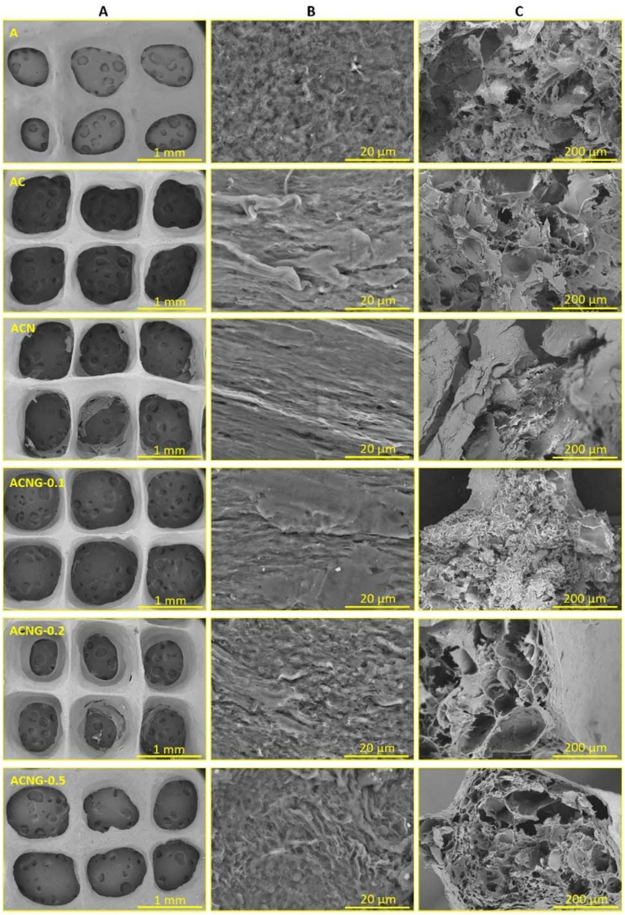

Fig. 3 (A) Top view, (B) surface and (C) cross-section SEM images obtained for the lyophilized scaffolds, at 1 mm, 20 μm and 200 μm scale.

aspect is desirable for the intended application because it was demonstrated that rough, irregular substrates favor cellular proliferation and differentiation, as opposed to smooth ones.[50] In the case of GO-containing scaffolds, the materials' porosity was slightly decreased, due to the deposition of carbonaceous fillers on the polymers surface and pore walls, as noticed in the cross-section micrographs (Fig. 3C). However, this was not considered a negative aspect, as the lower porosity was translated into improved printability and mechanical properties, particularly for the ACNG-0.1 sample. In a research conducted by Ajeel *et al.* a decrease in porosity of composite alginate/GO beads after the addition of filler was also observed, concluding that it was due to the tight bonding between alginate and GO, thus confirming the compatibility between the two components.[51] In our study, as the GO concentration was increased, the filler showed an agglomeration tendency, forming small aggregates randomly disposed on the scaffold surface (Fig. 3B); this confirmed the fact that uneven dispersion and agglomeration of GO sheets were the cause of difficult printing process in the case of ACNG-0.2 and ACNG-0.5 samples, according to the printability evaluation results (Fig. 2) and video recordings provided in the ESI (SI1†).

Morphological investigations by μ-CT analysis

Micro-computer tomography (μ-CT) was utilized to quantitatively and qualitatively evaluate both the 2D and 3D characteristics of the materials. Thanks to the contrast provided by the tomograms, it was possible to achieve clear distinctions of the discontinuous phases clustered above the scanning detection limit *vs.* the composite as a whole for separate measurements and discussions. There were clear centers within the fibers and GO-containing compositions, where the solid material was densely packed, forming elongated patterns of varying sizes and lengths, resembling fiber-like structures. None of the fibers utilized in the synthesis should be individually detectable at the scanning resolution, but their physical interactions promote their accumulation and the engrossing of calcium alginate chains. This resulted in the creation of regions with increased density, which exhibited enhanced X-ray absorption. These regions could be observed as lighter shades of gray in the upper portion of the gray-tone histogram (Fig. 4B). The discussion is made for the bulk composite (BC) and the fiber-dense domain (FDD) extracted from the initial tomograms after thresholding. BC is addressed in terms of porosity, while surface features and degree of anisotropy are discussed side by side for BC and FDD.

The total porosity (T.Po) of the printed materials was analyzed and their share depicted in Fig. 4, *vs.* the solid phase split into two components, FDD and BC, with the exception of A sample where no filler content was added, enabled by the contrast in the tomograms. In addition, based on the scanning resolution, pore, FDD and wall thickness distributions were calculated and displayed in the adjacent charts. Most of the FDDs occur in clusters below 9 μm, while the pore domain seems to narrow with the increase in filler content and distribute in a Gaussian pattern. The wall thickness, nonetheless, varies less, and usually reaches values of 38–42 μm. Based on these profiles, geometrical averaging was used to calculate the median wall/pore diameter (12.7/14.4 μm in sample A, 14.2/28.1 μm in sample AC, 17.2/20.2 μm in sample ACN, 12.6/15.1 μm in sample ACNG-0.1, 13.4/12.1 μm in sample ACNG-0.2 and 13.4/15.2 μm in sample ACNG-0.5); there are not significant gaps in the geometrics of wall/pore templates, indicating that all compositions exhibit equilibrated features. Interestingly, though, the T.Po varied considerably, from the least (72%) in ACNG-0.2 to the highest (89%) in AC. This suggests that there are particular solid phase interactions established between the ink components that can tailor how the freeze-drying process impact liquid/solid phase separation.

As previously stated, we do not expect to capture all the FDDs and neither refer to those as solely consisting of fibers (±GO agglomeration) since they are bound to form aggregates with the matrix too. However, we investigated the FDD to BC ratio in the five compositions and performed some volumetric and dimensional assessments. The fillers to matrix ratio in the synthesis should be around 20 : 80 (w/w). Based on the pie-charts inset values, illustrated ratios (v/v) increased in the following order: 1.7% in ACNG-0.1 < 3.3% in ACNG-0.2 < 3.5% in ACN < 5.2% in ACNG-0.5 < 6.9% in AC, compared to the total solid phase. The significantly off value of 1.7% could be attributed to a sort of filler structuration at that concentrations that favor their coherent assembly throughout the material, in domains mostly below the detection limit, interaction type that was in favor of a smooth printing process, as also observed in both rheological and printability studies. The other GO composites do not exhibit the same behavior, probably as a result of too many π–π interactions that could not be outreached by the electrostatic interactions of the fibers with the sheets, thus forming rather thicker FDDs.

The connection index (Conn.) is essential for characterizing the micro-architectural features that underlie complex biological and synthetic systems' physical and functional behavior, analyzing the structural integrity and interconnectivity of porous constructs, essential for characterizing their mechanical qualities. Conn. is calculated using 3D μ-CT images to count the nodes in the network, taking into account their size and shape. This metric usually assesses bone and porous material quality in clinical and research contexts, but the calculation can be adjusted to describe the arrangement of X-ray distinctive phases within the composite materials. Generally, a robust, more interrelated framework has a higher connection index which is reflected in its mechanical stability and lower fracture risk while fragmented and weaker structures corroborate with lesser indexes.

A high Conn. paired with a positive Euler number (E.n) provides a distinctive and somewhat paradoxical insight into the structure being analyzed, since it describes numerous interconnections, as well as significant number of isolated components which do not form intricate loops or enclosed spaces. In the design of the fiber reinforced composite inks we considered a potential adaptation of the individual phases with respect to the rest while reaching equilibrium; upon balancing the physical interactions that occur, a harmonious distribution

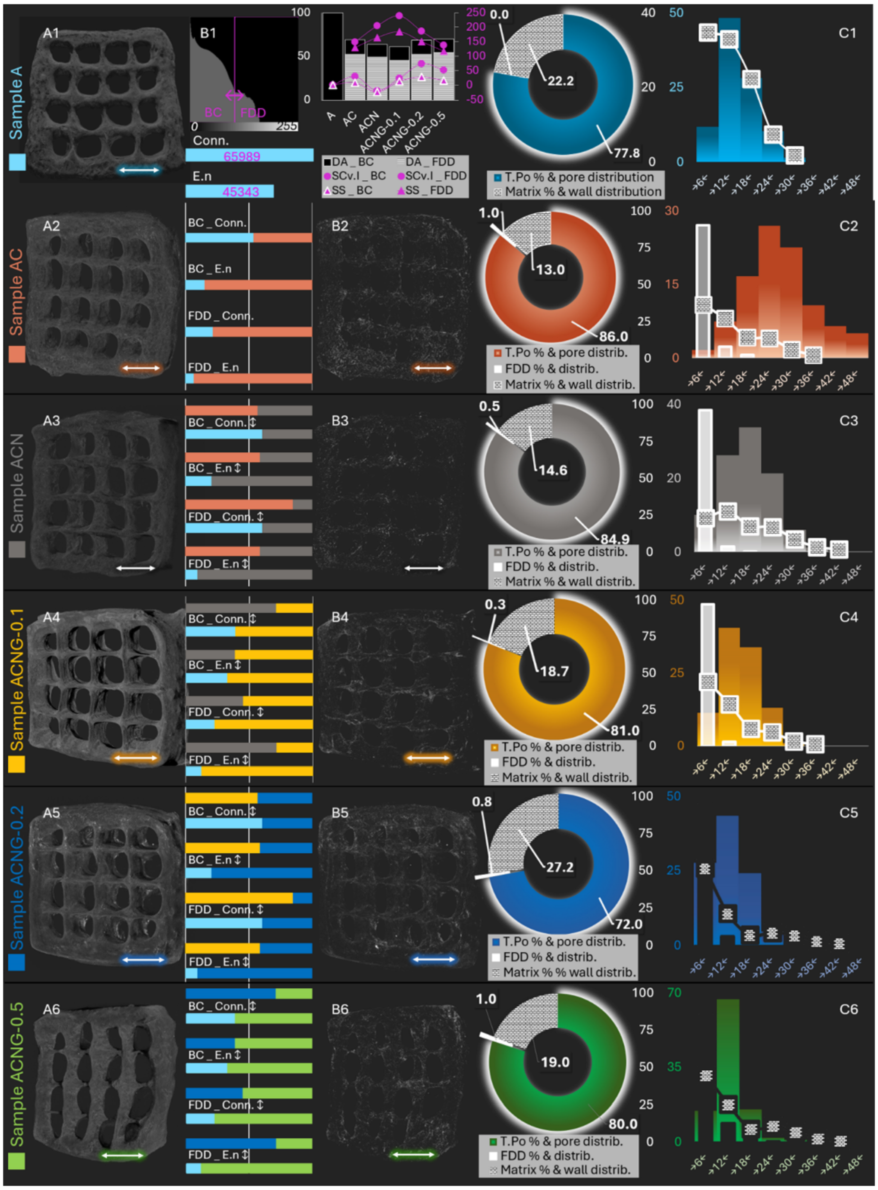

Fig. 4 Quantitative and qualitative μ-CT analysis. (A1–A6) subsets depict the tomograms of BC scanned objects, (B1) – grayscale histogram with thresholding defining the FDDs out of the BC scaffold volumes and numerical analysis performed for the 6 datasets (variations in DA, SCv.I), (B2–B6) illustrate the tomograms of the FDD, (C1–C6) total porosity, pore size distribution, FDD and BS thickness distributions. The double arrow scalebars in sections (A and B) cover a length of 2 mm in the samples. In subsections (C), the *x* axis depicts the median size of the domains in μm (3–9; 9–15, …, 42–54) while on the y the incident percentage (%) – coloured values associated to the pore size incidence.

of stresses and strains should be reached across the composite as a result of the geometrical configuration of the fillers.

This is the confirmation that our engineered biomaterials kept their intended design to have high connectivity for mechanical strength with minimal structural complexity for specific functional needs, like guided support for tissue formation. Data showed that there is a synergistic effect of the reinforcing and functional fibers addition, as well as of the GO sheets that seem to govern materials structure. The dispersed phases interact strongly in a compensatory mechanism that most probably keeps them interconnected and spatially oriented despite being dispersed within the polymer solution. The two focal points of the FDD tomograms (Fig. 4B2/C2–B6/C6) displayed these isolated distributions, but due to their elongated aspect, it seems that form a rather organized template confined within the ink deposition pathway. The tomograms of the fillers mainly illustrated the largest fiber agglomerates that were not fully interconnected, but since usually around 90% coalesce into structures of less than 9 μm, we believe that there is an important share that were under the scanning resolution of the equipment which engages with these observed entities at a micron-scale level. Despite the lesser level of complexity, this kind of micro-architectural feature can underpin efficient support and loads distribution.

Conn. and E.n were primarily discussed with respect to the ones measured for the control, but since each composition is a build-up on the former, their variations could be analyzed from two standpoints. The charts overlaid on Fig. 4B2/C2–B6/C6 depict the variations occurring with the compositing *vs.* control and *vs.* the previous formulation, so as to understand how the structure changes with each new addition (CNF, NF, GO) and GO concentration increase (0.1, 0.2, 0.5%). An indication that either Conn. or E.n decreased is the extent of the left-side bars (controls) exceeding the median gridline. Even though further analysis is needed for a more precise analysis of side-by-side pairs, when compared to the A control, up to ACNG-0.2 increasingly more connected scaffolds (BCs) and supra-structuration of FDDs emerged.

Surface convexity index (SCv.I) and object surface/volume ratio (specific surface – SS) were paired in the texture characterization of the six printable formulations. Both features varied similarly; plotted results are depicted in Fig. 4C1 with trendlines. Regarding the SCv.I, data revealed interesting progression of the surface complexity as a result of CNFs, NFs and GO sheets addition. The BCs exhibited a slightly rougher surface because of CNFs and smoothed out drastically for the NFs formulation. No linear correlation could be identified between GO ratio, but SCv.I increased in ACNG-0.1 and ACNG-0.2, which could also be observed in the SEM images, while in ACNG-0.5 roughness index appeared to decrease again, probably due to the stronger stacking interaction of GO sheets when higher concentration was used. On the other hand, FDDs feature increasingly rougher morphologies upon the addition of the first ratio of GO and get smoother for 0.2% and 0.5% since probably the carbon sheets tend to envelop the fibers and reduce specific protrusions of their assembly. The only major discrepancy in the trendlines was observed in ACN composition, which was probably caused by the extra-fiber content that co-assembles with the CNFs and onto which the calcium alginate uniformly adheres. As prior stated, the SS follows a comparable pattern. For both BCs and FDDs, SS and SCv.I reach maximum that can be associated with a possible upper limit of total filler content above which the dispersion is too concentrated to maintain its stability and abrupt phase separations occur. This was very well supported by the clearly broader distribution of FDD in ACNG-0.5.

The algorithm employed for determining the degree of anisotropy (DA) examines the directional alignment of the matter in the prints. Essentially, it quantifies the directional variation of structural qualities, such as stiffness or strength, by assessing the dependency and uniform distribution of the structural center of mass within the item. To further understand the phase structure inside the formulations, we conducted DA measurements for BC and FDD and examined their correlation. The pristine sample (A) exhibited the highest value (DA = 2.26), suggesting that the polymer structures are highly aligned in particular directions upon extrusion. This alignment could enhance the polymer's performance in terms of tensile strength, stiffness, and other properties along those specific directions. The rest of the batch had considerably lower DAs due to a more evenly distributed arrangement of reinforcing compounds, making the formulations more suitable for applications that involve multidirectional mechanical loads.

This could potentially enhance the cellular behavior throughout different stages of tissue formation and facilitate co-culturing of progenitor lineages that are responsive to specific micro-mechanical stimuli. The BCs' DAs were standardized and represented in Fig. 4 as a percentage of the DA value of the control. The lowest DA was observed in ACNG-0.1, and there was a tendency for an increase in DA for the other GO composites, which reaffirms the significance of the combined effect of 1D and 2D fillers, however, only up to a (probably total wt%) point. With respect to fillers, they exhibited lower values, which confirms their contribution to the structuring of the BC and their ability to disperse favorably inside the calcium alginate matrix. The variation of FDDs' exhibited a similar pattern to that of the BCs' and was consistently lower, averaging 22–25% less than the objects.

Structural analysis

The ATR FT-IR analysis was performed to investigate the interactions that occur between the calcium alginate (A) matrix and CNFs, NFs and GO fillers (Fig. 5B). As showed in Fig. 5A, the

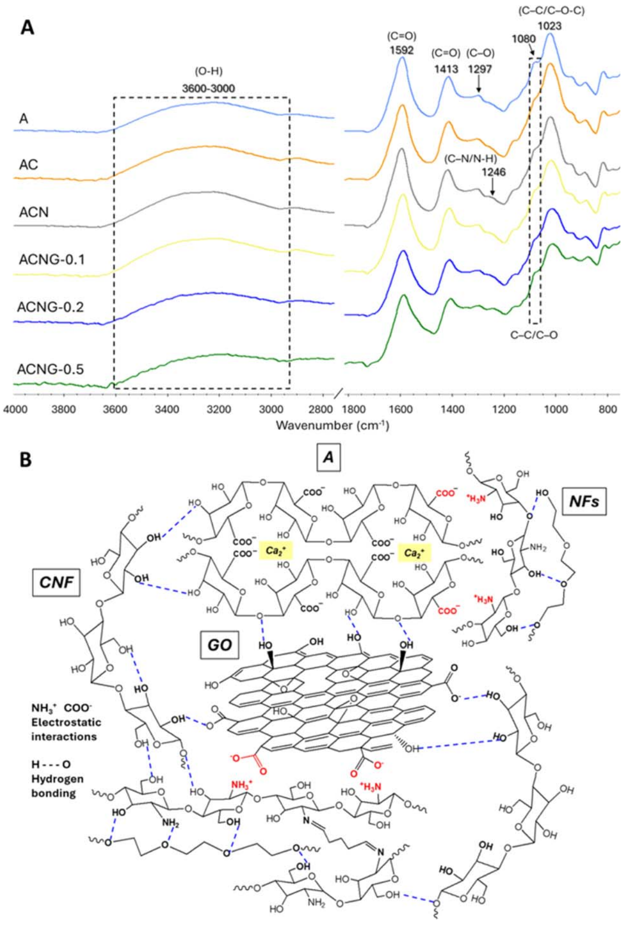

Fig. 5 (A) ATR FT-IR spectra of the analyzed materials; (B) schematic representation of various types of interactions between the functional groups of the components used in the design of composite scaffolds. Abbreviations: A – calcium alginate, CNF – cellulose nanofibrils, NFs – chitosan/poly(ethylene oxide) nanofibers, GO – graphene oxide.

FT-IR spectrum of A sample presents a large absorption band between 3600–3000 cm^{-1} corresponding to the stretching vibration of the OH groups, two well-defined peaks at 1592 and 1413 cm^{-1} generated by the asymmetric and symmetric stretching vibrations of the C═O groups, and a shoulder at 1080 cm^{-1} related to the C–C and C–O stretching, all of them being characteristic to the ionic bonds established between the Ca^{2+} ions and sodium alginate during the ionic gelation process. Finally, the peaks at 1297 cm^{-1} and 1023 cm^{-1} were associated with C–O and C–C/C–O–C stretching vibrations, respectively. All results were in good agreement with the ones previously reported in literature for calcium alginate.[52–54] No major changes were observed in the spectra of AC and ACN composites, most likely due to the overlapping of CNFs and NFs characteristic peaks by the ones belonging to the calcium alginate. Still, in the case of AC, the lower intensity of the shoulder located at 1080 cm^{-1} could be attributed to the non-covalent bonding (hydrogen bonds) between the –COOH and –OH groups of A and –OH of CNF,[55] while in the ACN spectrum, the presence of NFs was signaled by an amide III specific shoulder at 1246 cm^{-1}, generated by C–N and N–H bonds stretching vibrations.[56] After GO was introduced in the materials structure, the –OH absorption bands broadened and shifted towards lower values. According to previous studies, this phenomenon occurs as a result of hydrogen bonds formation and interfacial adhesion between calcium alginate and GO.[20,57]

Nanomechanical properties evaluation

Since the mechanical features of a scaffold have an important influence on the cellular behavior, nanoindentation technique was employed to determine the storage (G') and loss (G'') moduli, respectively elasticity and viscosity of the calcium alginate-based biomaterials. As expected, due to the hydrogel nature of the polymer matrix, G' values were higher than G'' for all the analyzed samples (Fig. 6), which is correlated with the rheological results.[58] After the CNFs, NFs and GO fillers were added, the general tendency was a gradual increase of both G' and G'', proportional to the filler content. The highest values were achieved by ACNG composites, particularly by ACNG-0.5 sample (G' = 172.10 kPa, G'' = 37.82 kPa), this suggesting a strong reinforcing effect of GO on the calcium alginate matrix. According to previous studies, the mechanical properties of the calcium alginate-based scaffolds were similar to the ones of the collagenous osteoid matrix, the precursor of the bone pre-calcification, which is basically the environment where stem cells proliferate and differentiate towards osteoblasts, this further confirming their biomimetic character.[59]

An interesting fact was that the filler addition could also increase the anisotropy degree of the scaffolds. Punctual differences in the G' and G'' values were observed in the case of all materials, and as fillers were added within the polymer matrix, the contrast between the values became higher. This phenomenon was most obvious in the case of ACN sample, where the standard deviation values corresponding to G' and G'' were 29.16 and 6.02, respectively. As mentioned before, the nanomechanical features of a material highly influence the cellular migration, proliferation and differentiation towards osteoblast lineages. The fact that after filler addition, the structural complexity (see μ-CT and SEM images) and mechanical anisotropy of the scaffolds are increased confirms the fact that these novel formulations are appropriate for replicating the complex natural bone ECM environment thus favoring bone tissue regeneration.

Thermal behavior

The DSC curves (Fig. 7) obtained for the alginate-based materials revealed that two major events took place upon heating process. The first event, represented by a strong endothermic peak located around 90–120 °C, depending on the material's composition (Table 3), was associated with the dehydration process of the polysaccharide molecules. There is a considerable difference regarding the maximum temperature at which the water loss occurs in each sample which may come from the supplementary interactions that take place between the components of the system. Thus, a higher dehydration temperature may suggest a higher crosslinking density or could indicate the formation of additional hydrogen bonds.[60] The second event took place at approximately 230 °C, with slight variations for each material (Table 3), and corresponded to the polymer melting process. Even if the melting temperatures were similar for all samples, it can be observed that the melting enthalpy increased with the addition of the fillers, the highest

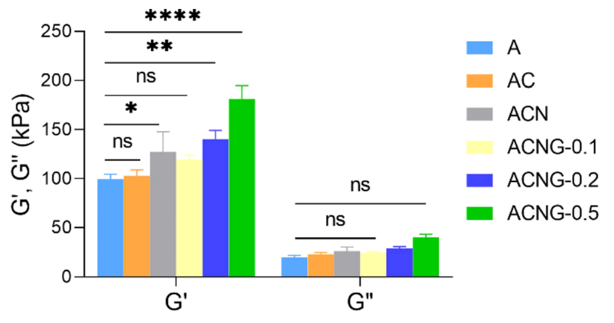

Fig. 6 Nanomechanical characteristics of the synthesized scaffolds, expressed by G' and G'' moduli (ns $p > 0.5$, *$p < 0.05$, **$p < 0.005$, ****$p < 0.0001$).

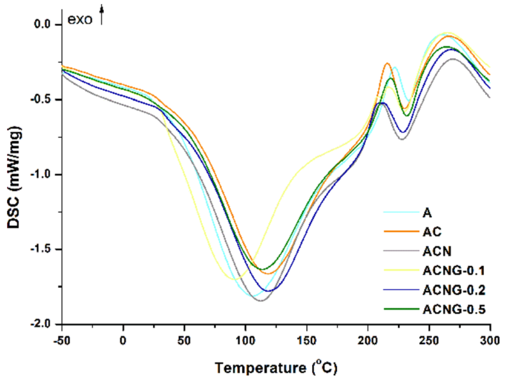

Fig. 7 DSC thermograms of the analyzed materials.

Table 3 Dehydration (T_1 max, ΔH_1) and melting (T_2 max, ΔH_2) temperatures and enthalpies of the analyzed materials extracted from DSC data

Sample	T_1 max (°C)	ΔH_1 (J g^{-1})	T_2 max (°C)	ΔH_2 (J g^{-1})
A	106.3	908.9	233.5	24.6
AC	118.2	780.6	229.9	44.5
ACN	112.5	791.4	228.1	54.1
ACNG-0.1	91.3	654.3	229.8	26.2
ACNG-0.2	118.5	686.8	228.7	40.2
ACNG-0.5	113.7	739.1	231.8	32.7

value being obtained for the ACN sample. Considering the fact that higher melting enthalpies are associated with an increased crystallinity degree,[60] it can be stated that the addition of the fillers induced a more organized character to the amorphous alginate matrix, most likely due to the interactions between the functional moieties on the fillers surface and the polymer chains.

In vitro swelling and degradation studies

The swelling degree (SD) was determined to investigate the behavior of calcium alginate-based scaffolds under physiological conditions (pH = 7.4, t = 37 °C). All materials showed a typical swelling behavior, characterized by a rapid fluid absorption within the first hour, depending on their composition, followed by an equilibrium phase with no substantial changes for the next 48 hours (Fig. 8A). The A sample showed the highest fluid uptake ability (MSD = 929.91%) followed by the ACNG-0.1 > ACNG-0.2 > ACN > AC > ACNG-0.5 composites (Fig. 8B). Still, the A sample also exhibited maximum swelling after only 20 minutes, compared to 50 minutes for AC and ACN, and 60 minutes for the GO-containing scaffolds. These results agree with previous nanoindentation study, showing that the materials' stability increases as fillers are added in their composition.[61] This behavior was expected because calcium alginate is a hydrophilic polymer and, as shown in the SEM images, the neat scaffold had a porous structure which is favorable for fluid uptake. After the filler's addition, the hydrogen bonds and interfacial interactions that occur between calcium alginate and CNFs, NFs, and GO, respectively, restrict the mobility of polymer chains, while the filler components deposit onto the materials surface and pore walls, thus reducing the overall porosity and preventing the diffusion of water molecules within the scaffold structure. Despite the MSD decrease (Fig. 8B), even the lowest value, that was reached by ACNG-0.5 composite (MSD = 811.08%), was still high enough to allow water diffusion and nutrients transport.[62] Moreover, the swelling suppression induced by filler addition is, in this case, beneficial, because it may help the scaffolds maintain their shape and mechanical properties in physiological environment.[63]

Another important aspect that needs to be considered when designing tissue engineering scaffolds is the biomaterial degradation rate, which, in the ideal case, should be balanced with the rate of novel ECM formation. If the degradation rate is too slow, new tissue formation could be hindered by the lack of space. Oppositely, if the degradation occurs to fast, the scaffold could lose its mechanical properties and initial structure, thus making it unable to provide appropriate support for tissue regeneration.[64] Considering that the initial healing phase of bone tissue takes approximately 6 to 12 weeks, this could be considered an adequate degradation timeframe for bone tissue engineering scaffolds.[65] As observed in Fig. 8C, the degradation degree (DD) of all samples had a sharp increase in the first 48 hours, followed by a constant degradation phase until the end of the experiment. The sample with the highest DD was A (20.1%), followed by ACN (14.90%), ACNG-0.1 (12.97%), ACNG-0.2 (12.44%), AC (12.30%) and ACNG-0.5 (11.37%). These results could be correlated with the structural and morphological features, swelling behavior and nanoindentation analysis, where it was also observed that the presence of fillers (especially GO) within the scaffolds' structure, improves their physical stability and mechanical properties. Moreover, since after 10 days, the DD was approximately 14% for all the composites (~1.4% per day), it can be postulated that the scaffolds could withstand in physiological environment and provide an adequate template for tissue formation throughout the 12 weeks, timeframe required for initial bone healing.

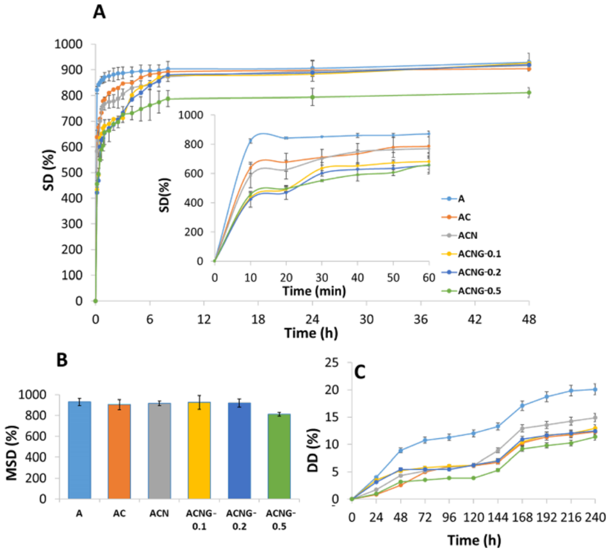

Fig. 8 (A) Swelling kinetics and (B) maximum swelling degree of the materials within 48 hours; (C) *in vitro* degradation curves obtained for the scaffolds within 240 hours.

In vitro biocompatibility

The MTT test results recorded after 4, 7 and 14 days demonstrated a cell viability of more than 70% for all the samples involved in the evaluation, which indicates a biocompatible behavior, according to the threshold described by the ISO10993-5:2009 standard "Biological Evaluation of Medical Devices-Part 5: Tests for *In vitro* Cytotoxicity". The biocompatibility of a scaffold for bone tissue regeneration is a vital issue, which determines the response of the cells to the presence of the implanted material and provides information about its prognosis in the host tissue. The MTT assay provides information on the total cell metabolism, as a result of direct contact between the osteoblast monolayer and the evaluated material. From the metabolic point of view, an increased viability is notable in the case of the sample with the highest amount of GO (ACNG-0.5) compared to the materials without GO, especially in the first days of incubation (ACNG-0.5 *vs.* A, *vs.* AC, *vs.* ACN) (Fig. 9A). A more pronounced cellular metabolism was also observed in the case of ACNG-0.2 and ACNG-0.5 materials compared to the samples without GO, after 7 and 14 days of incubation, but the effect was not statistically significant. These observations are supported by other results from specialized literature that confirmed the fact that GO has an osteostimulatory character and accelerates the metabolism of osteoblast cells.[26,66] It was also noticed that by increasing the material stiffness, the total cellular metabolism slightly decreased, a phenomenon that could be associated with the cellular differentiation.

A complementary test that evaluates the biocompatibility/cytotoxicity of an implant is the lactate dehydrogenase (LDH) release assay. After 4 days of incubation, no notable release of LDH in the extracellular environment was observed, the tendency being maintained after 7 and 14 days (Fig. 9B). These results confirmed the biocompatibility of the calcium alginate-based scaffolds on the osteoblast cells, for up to two weeks of incubation.

The process of bone differentiation is associated with progressive osteoid mineralization, which can be quantified using a method of specific marking of Ca deposits within the ECM of the osteoblast culture with Alizarin Red dye. After 4 days of incubation in the presence of scaffolds, a statistically significant increase in mineralization was observed in the samples, where the printability was improved by CNFs addition, compared to the A sample (A *vs.* ACN) (Fig. 9C). Also, increasing the scaffolds' stiffness induced a significant stimulation of ECM mineralization for the osteoblast cultures incubated in the presence of ACN. The GO addition within the material composition enhanced the calcification effect, even after 4 days of incubation. A statistically significant effect was observed for the sample with the lowest concentration of GO (ACNG-0.1) compared to the A control and NC. The stimulatory effect of osteoblast mineralization following incubation in the presence of composite scaffolds (ACNG-0.2 and ACNG-0.5) was significantly higher compared to A sample, after 7 days of incubation. After two weeks, the degree of mineralization was slightly increased, and a statistically significant improvement in the formation of Ca deposits was observed for the cell cultures exposed to the sample with the lowest concentration of GO (ACNG-0.1 *vs.* NC), this result confirming the potential of GO in stimulating osteoblasts differentiation.[67,68]

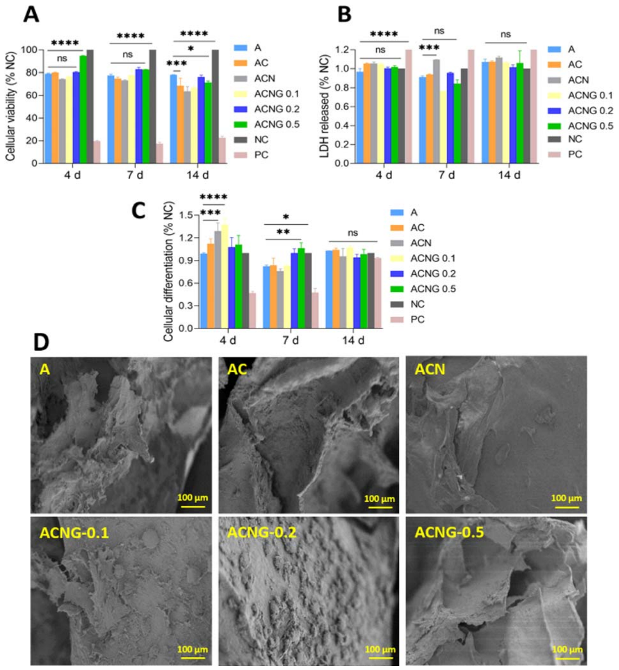

Fig. 9 (A) MTT, (B) LDH and (C) Alizarin Red assays results, obtained for MG-63 cells after 4, 7 and 14 days of incubation with the materials (ns $p > 0.5$, *$p < 0.05$, **$p < 0.005$, ***$p < 0.0005$, ****$p < 0.0001$); (D) SEM images of the osteoblast cultures exposed by direct contact with the samples for 4 days.

The cross-section SEM images achieved during the *in vitro* assays (Fig. 9D), confirmed that all the analyzed samples had a good biocompatibility with the MG-63 osteoblast cultures. The cells tightly adhered to the substrates, covering the entire available surface, and presented a typical osteoblast morphology with polygonal shape and fusiform cytoplasmic extensions that facilitate cellular adhesion to the scaffold.[69] Moreover, the orientation of the cells followed the scaffold morphology, and a preferential deposition on the nanofibers' bundles (areas with higher stiffness) was noticed in the case of the composite materials. The highest percentage of cellular adhesion was reached by the ACNG-0.1, this being in good agreement with the results obtained from MTT, LDH and Alizarin Red assays. In the case of A and AC samples, the presence of degradation products resulting from the scaffolds' decomposition following incubation in the complex cell culture medium, was observed. This phenomenon was diminished because of increasing the material stiffness by adding NFs and disappeared completely after the GO introduction within the composition, thus confirming the increase in chemical stability induced by filler addition; this was also noticed during the *in vitro* swelling and degradation studies.

Conclusions

This research work was focused on the design and fabrication of anisotropic and porous scaffolds for bone tissue engineering applications, using calcium alginate and cellulose nanofibers as polymer matrix, and electrospun chitosan/polyethylene oxide nanofibers and graphene oxide as functional fillers; these biomimicking scaffolds were engineered using the 3D printing technology.

ATR FT-IR analysis results showed that there was a good compatibility between the scaffold components, electrostatic interactions, hydrogen bonds and interfacial adhesion being established between calcium alginate and CNFs, NFs and GO, respectively. Furthermore, the nanoindentation, rheology and ink printability assessments showed that the addition of CNFs, NFs and low concentrations of GO (0.1%) induced solid-like behavior in calcium alginate composites and improved their mechanical features, printability index, expansion ration and uniformity factor. These results were also supported by the *in vitro* swelling and degradation studies, where the ACNG-0.1 scaffolds were found to be most stable. SEM and μ-CT images confirmed that the desired porous, anisotropic morphology was achieved, and the overall architecture of the composite scaffolds was similar to the one of natural bone ECM. Moreover, during the nanoindentation tests, significant differences were noticed between the values of the elasticity and viscosity moduli measured in different points on the composite materials surface, this further highlighting their anisotropic character. Finally, MTT, LDH and Alizarin Red assays confirmed the scaffolds' biocompatibility with MG-63 osteoblasts and emphasized that 0.1 wt% GO was the ideal concentration for enhancing cellular proliferation, differentiation and ECM mineralization. In virtue of these results, it can be concluded that the calcium alginate/cellulose nanofibrils-based 3D printed scaffolds double-reinforced with electrospun NFs and GO showed a great potential for bone tissue engineering applications.

Data availability

The authors confirm that the data supporting the findings of this study are available within the article and/or ESI.†

Author contributions

Elena Cojocaru: conceptualization, methodology, validation, formal analysis, investigation, writing – original draft, writing – review and editing, visualization; Mădălina Oprea: validation, formal analysis, writing – original draft, writing – review and editing; George Mihail Vlăsceanu: formal analysis, investigation, writing – original draft; Alin-Georgian Toader: formal analysis, investigation; Mădălina-Cristina Nicolae: formal analysis, investigation, writing – original draft; Roxana-Cristina Popescu: investigation, formal analysis, writing – original draft; Paul-Emil Mereuţă: formal analysis, investigation; Mariana Ioniţă: conceptualization, methodology, validation, writing – review and editing, supervision, project administration, funding acquisition.

Conflicts of interest

There are no conflicts to declare.

Acknowledgements

This work was funded by the EU's NextGenerationEU instrument through the National Recovery and Resilience Plan of Romania – Pillar III-C9-I8, managed by the Ministry of Research, Innovation and Digitalization, within the project entitled "Advanced & personalized solutions for bone regeneration and complications associated with multiple myeloma, contract no. 760093/23.05.2023, code CF 213/29.11.2022" and by a grant of the Ministry of Research, Innovation and Digitization, Executive Agency for Higher Education, Research, Development and Innovation, project number PCE 103/2022 (REOSTEOKIT).

References

1 G. Office of the Surgeon, in *Bone Health and Osteoporosis: A Report of the Surgeon General*, Office of the Surgeon General (US), Rockville (MD), 2004.

2 F. Schulze, A. Lang, J. Schoon, G. I. Wassilew and J. Reichert, *Biomedicines*, 2023, **11**(2), 325.

3 A. I. Cernencu, G. M. Vlasceanu, A. Serafim, G. Pircalabioru and M. Ionita, *RSC Adv.*, 2023, **13**, 24053–24063.

4 S. S. Lee, X. Du, I. Kim and S. J. Ferguson, *Matter*, 2022, **5**, 2722–2759.

5 H. Qu, H. Fu, Z. Han and Y. Sun, *RSC Adv.*, 2019, **9**, 26252–26262.

6 N. K. Nga, L. T. T. Tam, N. T. Ha, P. H. Viet and T. Q. Huy, *RSC Adv.*, 2020, **10**, 43045–43057.

7 X. Lin, S. Patil, Y. G. Gao and A. Qian, *Front. Pharmacol.*, 2020, **11**, 757.

8 N. Alcorta-Sevillano, I. Macías, A. Infante and C. I. Rodríguez, *Cells*, 2020, **9**(12), 2630.

9 A. E. Goodship and R. K. W. Smith, in *Equine Exercise Physiology*, ed. K. W. Hinchcliff, R. J. Geor and A. J. Kaneps, W. B. Saunders, Edinburgh, 2008, pp. 81–105, DOI: 10.1016/B978-070202857-1.50006-8.

10 T. Ishimoto, B. Sato, J.-W. Lee and T. Nakano, *Bone*, 2017, **103**, 216–223.

11 M. Whang and J. Kim, *Tissue Eng. Regener. Med.*, 2016, **13**, 126–139.

12 A. Shellard and R. Mayor, *Dev. Cell*, 2021, **56**, 227–239.

13 J. A. Espina, C. L. Marchant and E. H. Barriga, *FEBS J.*, 2022, **289**, 2736–2754.

14 J. Serrano-Bello, I. Cruz-Maya, F. Suaste-Olmos, P. González-Alva, R. Altobelli, L. Ambrosio, L. A. Medina, V. Guarino and M. A. Alvarez-Perez, *Front. Bioeng. Biotechnol.*, 2020, **8**, 587.

15 B. Yi, Q. Xu and W. Liu, *Bioact. Mater.*, 2022, **15**, 82–102.

16 G. Funda, S. Taschieri, G. A. Bruno, E. Grecchi, S. Paolo, D. Girolamo and M. Del Fabbro, *Materials*, 2020, **13**, 201.

17 M. Yazdanian, M. Alam, K. Abbasi, M. Rahbar, A. Farjood, E. Tahmasebi, H. Tebyaniyan, R. Ranjbar and A. Hesam Arefi, *Front. Bioeng. Biotechnol.*, 2022, **10**, 987195.

18 P. M. Sivakumar, A. A. Yetisgin, S. B. Sahin, E. Demir and S. Cetinel, *Carbohydr. Polym.*, 2022, **283**, 119142.

19 Y. Luo, A. Lode, A. R. Akkineni and M. Gelinsky, *RSC Adv.*, 2015, **5**, 43480–43488.

20 M. Ionita, M. A. Pandele and H. Iovu, *Carbohydr. Polym.*, 2013, **94**, 339–344.

21 R. Olmos-Juste, B. Alonso-Lerma, R. Pérez-Jiménez, N. Gabilondo and A. Eceiza, *Carbohydr. Polym.*, 2021, **264**, 118026.

22 S. Cui, S. Zhang and S. Coseri, *Carbohydr. Polym.*, 2023, **300**, 120243.

23 R. E. Abouzeid, R. Khiari, D. Beneventi and A. Dufresne, *Biomacromolecules*, 2018, **19**, 4442–4452.

24 M. Witzler, D. Büchner, S. Shoushrah, P. Babczyk, J. Baranova, S. Witzleben, E. Tobiasch and M. Schulze, *Biomolecules*, 2019, **9**, 840.

25 G. M. Vlăsceanu, H. Iovu and M. Ioniţă, *Composites, Part B*, 2019, **162**, 712–723.

26 E. A. Chiticaru and M. Ionita, *FlatChem*, 2022, **35**, 100417.

27 A. Şelaru, H. Herman, G. M. Vlăsceanu, S. Dinescu, S. Gharbia, C. Baltă, M. Roşu, C. V. Mihali, M. Ioniţă, A. Serafim, H. Iovu, A. Hermenean and M. Costache, *Int. J. Mol. Sci.*, 2022, **23**(1), 491.

28 M. Oprea and S. I. Voicu, *Materials*, 2020, **13**, 5347.

29 Y. Hu, H. Zhang, H. Wei, H. Cheng, J. Cai, X. Chen, L. Xia, H. Wang and R. Chai, *Eng. Regen.*, 2022, **3**, 154–162.

30 E. Cojocaru, J. Ghitman, E. I. Biru, G. G. Pircalabioru, E. Vasile and H. Iovu, *Materials*, 2021, **14**, 2535.

31 W. Ma, S. Zhang, C. Xie, X. Wan, X. Li, K. Chen and G. Zhao, *Polymers*, 2022, **14**, 2083.

32 F. Tao, Y. Cheng, X. Shi, H. Zheng, Y. Du, W. Xiang and H. Deng, *Carbohydr. Polym.*, 2020, **230**, 115658.

33 J. Jeevanandam, S. Pan, J. Rodrigues, M. A. Elkodous and M. K. Danquah, *Biomater. Sci.*, 2022, **10**, 4107–4118.

34 S. Im, G. Choe, J. M. Seok, S. J. Yeo, J. H. Lee, W. D. Kim, J. Y. Lee and S. A. Park, *Int. J. Biol. Macromol.*, 2022, **205**, 520–529.

35 Q. Gao, X. Niu, L. Shao, L. Zhou, Z. Lin, A. Sun, J. Fu, Z. Chen, J. Hu and Y. Liu, *Biofabrication*, 2019, **11**, 035006.

36 S. D. Dutta, J. Hexiu, D. K. Patel, K. Ganguly and K.-T. Lim, *Int. J. Biol. Macromol.*, 2021, **167**, 644–658.

37 K. Chatterjee, S. Lin-Gibson, W. E. Wallace, S. H. Parekh, Y. J. Lee, M. T. Cicerone, M. F. Young and C. G. Simon Jr, *Biomaterials*, 2010, **31**, 5051–5062.

38 A. Kroll, M. H. Pillukat, D. Hahn and J. Schnekenburger, *Eur. J. Pharm. Biopharm.*, 2009, **72**, 370–377.

39 M. E. Cooke and D. H. Rosenzweig, *APL Bioeng.*, 2021, **5**, 011502.

40 H. Herrada-Manchón, M. A. Fernández and E. Aguilar, *Gels*, 2023, **9**, 517.

41 K. Markandan, I. P. Seetoh and C. Q. Lai, *J. Mater. Res.*, 2021, **36**, 4262–4274.

42 R. Eqra, M. H. Moghim and N. Eqra, *Polym. Polym. Compos.*, 2021, **29**, S556–S564.

43 M. Albozahid, S. A. Habeeb, N. A. Ismael Alhilo and A. Saiani, *Mater. Res. Express*, 2020, **7**, 12.

44 J. Li, X. Liu, J. M. Crook and G. G. Wallace, *Front. Bioeng. Biotechnol.*, 2022, **10**, 1–10.

45 X. Wei, D. Li, W. Jiang, Z. Gu, X. Wang, Z. Zhang and Z. Sun, *Sci. Rep.*, 2015, **5**, 11181.

46 Q. Ma, K. Wang, D. Mohawk, A. Mahoney, Y. Chen and L. Jiang, *Ind. Crops Prod.*, 2024, **209**, 118000.

47 N. Bahrami, A. Farzin, F. Bayat, A. Goodarzi, M. Salehi, R. Karimi, A. Mohamadnia, A. Parhiz and J. Ai, *Arch. Neurosci.*, 2019, **6**, e85122.

48 R.-i. Nakayama, Y. Takamatsu and N. Namiki, *SN Appl. Sci.*, 2020, **2**, 1799.

49 M. A. Ibrahim, M. H. Alhalafi, E.-A. M. Emam, H. Ibrahim and R. M. Mosaad, *Polymers*, 2023, **15**, 2820.

50 L. Zhu, D. Luo and Y. Liu, *Int. J. Oral Sci.*, 2020, **12**, 6.

51 S. J. Ajeel, A. A. Beddai and A. M. N. Almohaisen, *Mater. Today: Proc.*, 2022, **51**, 289–297.

52 Q. Liu, Q. Li, S. Xu, Q. Zheng and X. Cao, *Polymers*, 2018, **10**, 664.

53 J. Nastaj, A. Przewłocka and M. Rajkowska-Myśliwiec, *Pol. J. Chem. Technol.*, 2016, **18**, 81–87.

54 A. Saarai, V. Kasparkova, T. Sedlacek and P. Saha, *J. Mech. Behav. Biomed. Mater.*, 2013, **18**, 152–166.

55 P. Siqueira, É. Siqueira, A. E. de Lima, G. Siqueira, A. D. Pinzón-Garcia, A. P. Lopes, M. E. C. Segura, A. Isaac, F. V. Pereira and V. R. Botaro, *Nanomaterials*, 2019, **9**(1), 78.

56 C. Chen, Z. Li, C. Wang, S. Liu, Y. Wang, M. Zhang, Y. Tian, J. Lv, H. Xu and G. Xia, *LWT*, 2023, **173**, 114335.

57 Y. Wan, X. Chen, G. Xiong, R. Guo and H. Luo, *Mater. Express*, 2014, **4**, 429–434.

58 E. Olaret, D. Steinmüller-Nethl, H. Iovu and I.-C. Stancu, *UPB Sci. Bull. Ser. B*, 2022, **84**(3), 27–40.

59 T. Jiang, M.-T. Zheng, R. M. Li and N. J. Ouyang, *Mechanobiology in Medicine*, 2024, **2**, 100046.

60 G. T. Padma, T. Subba Rao and K. Chandra Babu Naidu, *SN Appl. Sci.*, 2018, **1**, 75.

61 N. Rehman, M. R. Dilshad, A. Islam, N. Gull, T. Riaz, S. M. Khan and R. U. Khan, *J. Drug Delivery Sci. Technol.*, 2021, **66**, 102784.

62 M. Oprea, D. M. Panaitescu, C. A. Nicolae, A. R. Gabor, A. N. Frone, V. Raditoiu, R. Trusca and A. Casarica, *Polym. Degrad. Stab.*, 2020, **179**, 109203.

63 J. Li, J. Ma, S. Chen, Y. Huang and J. He, *Mater. Sci. Eng., C*, 2018, **89**, 25–32.

64 X. Barceló, K. F. Eichholz, O. Garcia and D. J. Kelly, *Biomedicines*, 2022, **10**(7), 1621.

65 H. ElHawary, A. Baradaran, J. Abi-Rafeh, J. Vorstenbosch, L. Xu and J. I. Efanov, *Semin. Plast. Surg.*, 2021, **35**, 198–203.

66 S. Dinescu, M. Ionita, A. M. Pandele, B. Galateanu, H. Iovu, A. Ardelean, M. Costache and A. Hermenean, *Bio-Med. Mater. Eng.*, 2014, **24**, 2249–2256.

67 M. Li, Y. Wang, Q. Liu, Q. Li, Y. Cheng, Y. Zheng, T. Xi and S. Wei, *J. Mater. Chem. B*, 2013, **1**, 475–484.

68 R. Huang, Y. Gu, Y. Yuan, Y. Wang, Y. Pan, B. Li, G. Ren, L. Huang and Y. Xie, *Front. Bioeng. Biotechnol.*, 2024, **12**, 1378681.

69 M. A. Sahebalzamani, M. Ziminska, H. O. McCarthy, T. J. Levingstone, N. J. Dunne and A. R. Hamilton, *Biomater. Sci.*, 2022, **10**, 2734–2758.